Effect of Coulomb Carrier Drag and Terahertz Plasma Instability in p^+-p-i-n-n^+ Graphene Tunneling Transistor Structures

V. Ryzhii,[1,2,*] M. Ryzhii,[3] A. Satou,[1] T. Otsuji,[1] V. Mitin,[4] and M.S. Shur[5]

[1] *Research Institute of Electrical Communication, Tohoku University, Sendai 980-8577, Japan*
[2] *Institute of Ultra High Frequency Semiconductor Electronics of RAS, Moscow 117105, Russia*
[3] *Department of Computer Science and Engineering, University of Aizu, Aizu-Wakamatsu 965-8580, Japan*
[4] *Department of Electrical Engineering, University at Buffalo, SUNY, Buffalo, New York 14260, USA*
[5] *Department of Electrical, Computer, and Systems Engineering, Rensselaer Polytechnic Institute, Troy, New York 12180, USA*

(Received 2 September 2021; revised 8 November 2021; accepted 8 December 2021; published 22 December 2021)

We evaluate the influence of Coulomb drag of electrons and holes in gated n and p regions caused by ballistic electrons and holes generated in a depleted i region due to interband tunneling on the current-voltage characteristics and impedance of p^+-p-i-n-n^+ graphene tunneling transistor structures (GTTSs). This drag leads to current amplification in the gated n and p regions and positive feedback between the amplified dragged current and the injected tunneling current. A sufficiently strong drag can result in a negative real part of the GTTS impedance, enabling a plasma instability and self-excitation of plasma oscillations in the terahertz (THz) frequency range. This effect might be used for the generation of THz radiation.

DOI: 10.1103/PhysRevApplied.16.064054

I. INTRODUCTION

Interband Zener-Klein tunneling in a depleted i region in p-i-n graphene diodes leads to the generation of holes and electrons, with holes propagating primarily in the direction of the built-in electric field and electrons propagating in the opposite direction [1–4]. If the i region is sufficiently short, the scattering of the carriers generated in this region on impurities and acoustic phonons is ineffective. As a result, the generated carriers propagate across such a region ballistically with a directed velocity close to the characteristic velocity $v_W \simeq 10^8$ cm/s. This very fast carrier transit can be used in several different ultrahigh-frequency devices operating at room temperature. In particular, p-i-n graphene diodes and p^+-p-i-n^+ graphene tunneling transistor structures (GTTSs) can exhibit negative dynamic conductivity [5,6], associated with a transit-time effect at frequencies close to the inverse transit time $v_W/2l_i$ (where $2l_i$ is the length of the depleted i region), which is in the range of several terahertz (THz) for submicrometer dimensions. Recently [7,8], we demonstrated that in graphene-based structures, ballistic carriers injected into a gated n region (or p region) can effectively drag [9–11] the equilibrium carriers. Because of the specifics of Coulomb carrier-carrier scattering in G layers having two-dimensional linear dispersion [9–14], the drag can be accompanied by a marked current amplification. This is because the injected ballistic carriers (BCs) colliding with the equilibrium carriers (ECs) transfer their momenta to the latter while keeping their directed velocity. As demonstrated previously [8], the Coulomb drag effect in G-based n^+-i-n-n^+ field-effect transistors (GBFETs) with injection of ballistic electrons from the source can enable a current-driven plasma instability and self-excitation of a source-drain current, leading to the emission of THz radiation.

In this paper, we consider reversed-biased p^+-p-i-n-n^+ GTTSs with gated p and n regions induced by negative and positive gate voltages $V_p < 0$ and $V_n > 0$, respectively, i.e., by so-called electrostatic doping.

Figure 1(a) shows GTTSs with applied gate voltages V_p and V_n ($-V_p = V_n = V_g > 0$) and a reverse bias voltage V between the side contacts. The voltages result in the depletion of the i region and creation of a sufficiently strong lateral electric field in this region to enable effective interband tunneling. Figures 1(b) and 1(c) show qualitatively band diagrams of GTTSs in the case of negligible Coulomb carrier drag (as in Ref. [5]) and in a case when this drag is substantial. In the first case, the potential distribution across the p and n regions is nearly flat due to the relatively high conductivity of these regions. However, since the drag of the equilibrium carriers caused by the injected ballistic carriers pushes out a fraction of the equilibrium carriers to the side contacts, to compensate these carriers

*v-ryzhii@riec.tohoku.ac.jp

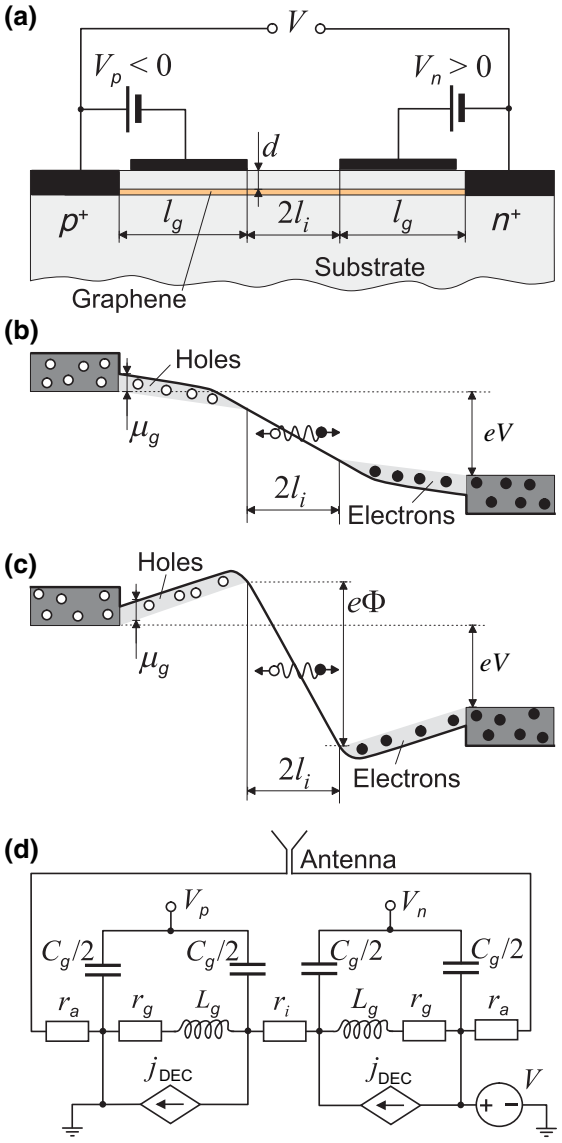

FIG. 1. (a) Cross section of a lateral p^+-i-n^+ GTTS with ballistic transport of tunneling-generated electrons and holes in the i region. Band diagrams (b) in the absence of drag current, $\Phi < V$, and (c) with a strong Coulomb carrier drag, $\Phi > V$. (d) Equivalent circuit of a GTTS, including an antenna with radiation resistance $2r_a$ (r_i is the resistance of the i region, and r_g, L_g, and C_g are the resistance, inductance, and capacitance, respectively, of the gated region). The current sources describe the dragged-equilibrium-carrier currents $j_{DEC} = J_{DEC}H$ (where H is the device width).

displaced from the gated regions (or to prevent such a displacement), lateral built-in electric fields in the p and n regions arise (corresponding to a marked inclination of the potential in the gated region). The GTTSs under consideration differ from the forward-biased GBFETs studied previously in that they have a different mechanism of ballistic-carrier generation (interband Zener-Klein tunneling in GTTSs versus thermionic space-charge-limited injection in GBFETs) and, hence, have different energy distributions of the carriers injected into the gated regions. This leads to different device characteristics, in particular, to different criteria for a plasma instability.

Using a device model developed by us, we calculate the dc current-voltage (I-V) characteristics and the small-signal impedance of a GTTS. In particular, we demonstrate that the real part of the impedance of a GTTS can be negative in a certain range of THz frequencies, structural parameters of the device, and bias voltages. The imaginary part of the impedance can become zero at the plasma frequency. These conditions can correspond to a plasma instability and to self-excitation of plasma oscillations converted to emitted THz radiation.

II. DEVICE MODEL

To consider GTTSs, we use the equivalent circuit of a GTTS shown in Fig. 1(d). Similar G-based structures with enhanced carrier mobility have been fabricated, experimentally studied, and well documented in the literature (see, for example, Refs. [15–23]).

In contrast to monopolar n^+-i-n-n^+ GBFETs using the drag effect associated with ballistic electrons thermally injected from the n^+ contact (space-charge limited injection) into the i region and then into the gated n region [7,8], here we consider GTTSs with electron and hole generation by interband tunneling across the entire i region (approximately spatially uniform). We analyze the drag caused by ballistic carriers with energies distributed over a wide range (from approximately zero energy for electrons or holes generated near the n or p region, respectively, to the energy $\varepsilon = eV$, where $e = |e|$ is the electron charge). We account for the asymmetric potential distribution and the contribution of carriers of both types to the device characteristics.

We assume that:

(i) The length, $2l_i$, of the depleted i region is sufficiently short to allow ballistic motion of the injected electrons: $2l_i \ll v_W\tau_i$, where τ_i is the characteristic time of BC scattering on disorder (acoustic phonons and impurities). As demonstrated [24], the latter condition can be satisfied for $2l_i \sim 1$ μm at room and lower temperatures in G layers encapsulated in h-BN [25].

(ii) The characteristic time, τ_{cc}, for the scattering of BCs on ECs is much shorter than the EC scattering time, τ_g, in the gated p and n regions: $\tau_{cc} \ll \tau_g$ (with the characteristic times for BC and EC scattering on disorder being approximately equal to each other, i.e., $\tau_g \sim \tau_i$). In this case, a substantial fraction of the momentum of the BCs can be transferred to the ECs, converting them into dragged ECs (DECs).

(iii) BCs that acquire an energy exceeding the threshold for optical-phonon emission (about the energy of optical phonons, $\hbar\omega_0 \simeq 0.2$ eV) are scattered primarily in the

gated regions with a relatively small characteristic time τ_0. The fraction of optical phonons emitted by the BCs in the depletion region is small if the potential drop across this region is smaller than $\hbar\omega_0$.

(iv) Because of the short length of the i region, the delay due to carrier transit, the capacitance, and the kinetic inductance of this region are disregarded.

For carrier densities $\Sigma_g \simeq 1 \times (10^{12}$–$10^{13})$ cm^{-2} and a temperature $T \lesssim 300$ K, and for the energy ε_{BC} of the BCs injected into the p and n regions, one can assume that $\tau_{cc} \lesssim 0.1$ ps. The characteristic times for scattering on disorder and on optical phonons are estimated as $\tau_g \simeq$ (1–2) ps and $\tau_0 \simeq$ (0.5–1.0) ps [26]. The use of electrostatic doping of the p and n regions allows one to minimize the ratio τ_{cc}/τ_g. The characteristic time for optical-phonon spontaneous emission is set to $\tau_0 \simeq$ (0.5–1.0) ps.

As can be seen from the GTTS equivalent circuit shown in Fig. 1(d), one needs to equalize the BC current across the i region (equal to the terminal current) and the net currents across the p and n regions (the Kirchhoff circuit law). As a result, we arrive at the following equation:

$$J_{BC} = J_{DEC} + J_{EC} + J_{DP}. \tag{1}$$

Here J_{BC}, J_{EC}, J_{DP}, and J_{DEC} are the densities of the BC current injected into the gated n region (or the gated p region), the EC current, the displacement current, and the DEC current in the gated region, respectively. These quantities are given by the following equations:

$$J_{BC} = \alpha_i \Phi^{3/2}, \tag{2}$$

$$J_{EC} = \sigma_g \frac{(V-\Phi)}{2l_g} - \frac{\mathcal{L}_g}{l_g}\frac{d\,J_{EC}}{dt}, \tag{3}$$

$$J_{DP} = c_g \frac{d(V-\Phi)}{dt}. \tag{4}$$

Here, $\alpha_i = e^{5/2}/2\pi^2\hbar^{3/2}\sqrt{2l_i v_W}$ (see Refs. [1–6]); $\sigma_g = e^2\Sigma_g\tau_g/m$ is the drift (Drude) conductivity; $c_g = l_g\kappa/8\pi d$ and $\mathcal{L}_g$ are the capacitance and the kinetic carrier inductance (per unit width of the GTTS in the lateral direction perpendicular to the terminal current) of the gated region; d and κ are the thickness of the gate layer and its dielectric constant; and $m_g = \mu_g/v_W^2 \simeq \hbar\sqrt{\pi\,\Sigma_g}/v_W^2$ and $\mu_g \simeq \hbar\, v_W\sqrt{\pi\,\Sigma_g}$ are the EC fictitious effective mass and the Fermi energy. The quantities Φ and $(V-\Phi)/2$ are the potential drops across the i region and the gated region.

The nonlinear dependence of the injected BC current density J_{BC} on the voltage drop Φ across the depleted region given by Eq. (2) originates from the specifics of the *interband* Zener-Klein tunneling [1–6]. Equation (3) represents the EC current density in the gated region corresponding to the Drude formula, accounting for the carrier kinetic inductance described by the second term on the right-hand side of this equation. The combination of the first and second terms leads to the standard frequency dependence of the Drude ac conductivity. The quantity J_{DP} governed by Eq. (4) is the displacement current density between the gate and the gated region of the electron (or hole) channel.

III. DEC CURRENT

To calculate the DEC current, we use an approach similar to that in Ref. [7], considering the features of BC injection into the gated regions in GTTSs associated with interband Zener-Klein tunneling [1–6]. We account for the fact that the DEC current is proportional to the flux of BCs entering the gated region, i.e., proportional to J_{BC}. Because of the linearity of the electron and hole energy-momentum dispersion laws, the average momentum that a BC transfers to the ECs due to carrier scattering in the gated region is equal to $e\Phi/2v_W$, i.e., according to Eq. (2), it is proportional to $J_{BC}^{2/3}$. Hence, $J_{DEC} \propto J_{BC}^{5/3}$. The momentum of BCs and DECs with an energy exceeding the optical-phonon energy $\hbar\omega_0$ is effectively dissipated due to the emission of such phonons. The emission of optical phonons strongly decreases the contribution of excessively hot BCs to the drag effect. This results in a steep drop in J_{DEC} when $e\Phi$ becomes sufficiently larger than $\hbar\omega_0$. As a result, we arrive at the following equation:

$$J_{DEC} \simeq b\frac{J_{BC}^{5/3}}{J_0^{2/3}}e^{-K}. \tag{5}$$

Here,

$$K = \frac{K_0}{2}\frac{[(e\Phi - \hbar\omega_0 + \mu_g)^2 - \mu_g^2]}{\hbar^2\omega_0^2}\Theta(e\Phi - \hbar\omega_0), \tag{6}$$

$K_g = l_g/v_W\tau_g$, $K_0 = l_g/v_W\tau_0$, and $K_{cc} = l_g/v_W\tau_{cc}$, with $K_g < K_0 \ll K_{cc}$.

The factor of 2 in the denominator occurs because the carriers injected into the gated region have an average energy equal to $e\Phi/2$. The dependence of K on the Fermi energy μ_g describes the effect of the population of the gated region on the energy threshold for optical-phonon emission caused by electrons and holes, which is reflected by the unity step function Θ with a threshold energy $\hbar\omega_0 + \mu_g$. Equation (6) accounts for this effect and the linear energy dependence of the density of states. The coefficient b in Eq. (5), which we call the Coulomb carrier drag factor, calculated accounting for the specifics of the carrier-carrier scattering kinematics in the case of linear energy-momentum dispersion relations for the carriers in G layers [7], is given by

$$b = \frac{\hbar\omega_0}{3T}\frac{\mathcal{F}_1(\mu_g/T)}{\mathcal{F}_2(\mu_g/T)}e^{-K_g} \simeq \frac{\hbar\omega_0}{2\mu_g}e^{-K_g} \lesssim \frac{\hbar\omega_0}{2\mu_g}, \tag{7}$$

where T and $\mathcal{F}_n(\xi) = \int_0^\infty du\, u^n[1+\exp(u-\xi)]^{-1}$ are the temperature (in energy units) and the Fermi-Dirac integral, respectively. For convenience, in Eq. (5), we introduce the characteristic current density

$$J_0 = \alpha_i \left(\frac{\hbar\omega_0}{e}\right)^{3/2}. \tag{8}$$

The quantity $J_{\rm DEC}$ is different from that calculated previously [7] for GBFETs with virtually monoenergetic BCs.

IV. dc CHARACTERISTICS

When a dc bias voltage $V = \overline{V}$ is applied between the side contacts, $\Phi = \overline{\Phi} = {\rm const}$, and the density of the terminal current is $J_{\rm BC} = \overline{J_{\rm BC}} = {\rm const}$. Introducing the normalized current density $J = \overline{J_{\rm BC}}/J_0$, from Eq. (1) we arrive at the following equation relating $\overline{J}$ and $\overline{V}$ (i.e., the GTTS I-V characteristic):

$$\overline{J} + \eta\overline{J}^{2/3} - b\overline{J}^{5/3}e^{-K(\overline{J})} = \eta\frac{\overline{V}}{V_0}, \tag{9}$$

where

$$\eta = \frac{\sigma_g}{2l_g\alpha_i\sqrt{V_0}} = \frac{\pi\tau_g\mu_g}{\hbar}\sqrt{\frac{2l_i v_W}{l_g^2\omega_0}} \tag{10}$$

is the ratio of the resistances of the i and g regions, and $V_0 = \hbar\omega_0/e$. In Eq. (9), we express the dc potential drop across the depleted region $\overline{\Phi}$ via $\overline{J}$, i.e., $\overline{\Phi} = \overline{J}V_0$. Taking this and Eq. (6) into account, we obtain

$$K(\overline{J}) = \frac{K_0}{2}[(\overline{J}^{2/3} - 1 + F)^2 - F^2]\Theta(\overline{J} - 1). \tag{11}$$

Analyzing Eq. (9), we find that for $b\Lambda \le 1 + 2\eta/3$, where

$$\Lambda = \left.\frac{d[J^{5/2}e^{-K(J)}]}{dJ}\right|_{J=\overline{J}}, \tag{12}$$

the GTTS I-V characteristics are monotonic. In this case, $\overline{\Phi} < \overline{V}$ [see Fig. 1(b)]. In the opposite case, when $b\Lambda > 1 + 2\eta/3$, the GTTS I-V characteristics become S-shaped, analogously to those demonstrated previously [7] (in devices with a different type of BC injection). In the latter case, $\overline{\Phi} > \overline{V}$ [see Fig. 1(c)].

When $\overline{J} \lesssim 1$, as follows from Eq. (11), $K(\overline{J}) \simeq$ const, and $\Lambda \simeq 5\overline{J}^{3/2}/2$. Considering this, the formation of S-shaped I-V characteristics requires

$$\frac{5}{2}b > 1 + \frac{2}{3}\eta, \tag{13}$$

while a sufficient condition for a monotonic shape of the I-V characteristics (despite the drag effect) can be presented as

$$\frac{5}{2}b < 1 + \frac{2}{3}\eta. \tag{14}$$

Figure 2 shows examples of I-V characteristics calculated using Eqs. (9) and (11) for different structural parameters. We set $\tau_0 = 0.5$ ps, $2l_i = 0.2$ μm, $l_g = 0.5$ μm, and $\tau_g = 1$ ps for $\mu_g = 50$ meV ($K_g = 0.5$) and $\tau_g = 2$ ps for $\mu_g = 15$ meV ($K_g = 0.25$). This implies that $K_0 = 2.0$. The I-V characteristic for $\mu_g = 50$ meV, which can be attributed to $T = 300$ K ($\mu_g/T \gtrsim 2$), rises monotonically. Very similar characteristics (virtually undistinguishable) are obtained for the Fermi-energy range $\mu_g = 40$–60 meV with $b \simeq 1.0$–1.5 and $\eta \simeq 10$–15. The latter implies that the inequality in Eq. (14) is well satisfied. Therefore the I-V characteristics for $\mu_g = 40$–60 meV are monotonic. For comparison, we calculate also the I-V characteristics corresponding to lower temperatures, setting the Fermi energy μ_g to 15 meV (the Fermi energy can be decreased by decreasing the gate voltage V_g). These data can be conditionally ascribed to $T = 77$ K with $\mu_g/T \gtrsim 2$. An example of the pertinent I-V characteristics, also shown in Fig. 2, exhibits a pronounced S shape. This characteristic corresponds to the parameters b and η satisfying the inequality in Eq. (13), which is opposite to the inequality in Eq. (14), i.e., a relatively large b and small η; in this case $b \simeq 5.19$ and $\eta \simeq 7.54$.

Figure 3 shows the quantity $b\Lambda$ as a function of the normalized bias current calculated using Eqs. (11) and (12). As can be seen from Fig. 3, the value of $b\Lambda$ depends explicitly on the structural parameters and the bias current. A crucial point is that $b\Lambda$ could markedly exceed unity, particularly for $\overline{J} \simeq 1$, with the parameters chosen above.

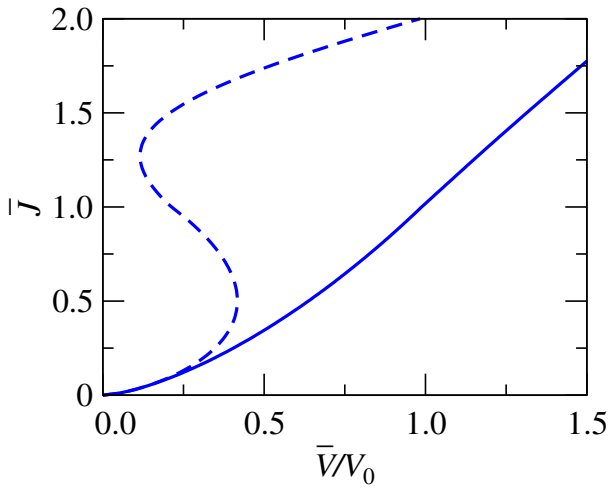

FIG. 2. Examples of GTTS I-V dc characteristics for different structural parameters: $l_g = 0.5$ μm, $\mu_g = 50$ meV, and $\tau_g = 1$ ps (solid line) (monotonic), and $l_g = 0.5$ μm, $\mu_g = 15$ meV, and $\tau_g = 2$ ps (dashed line) (S-shaped).

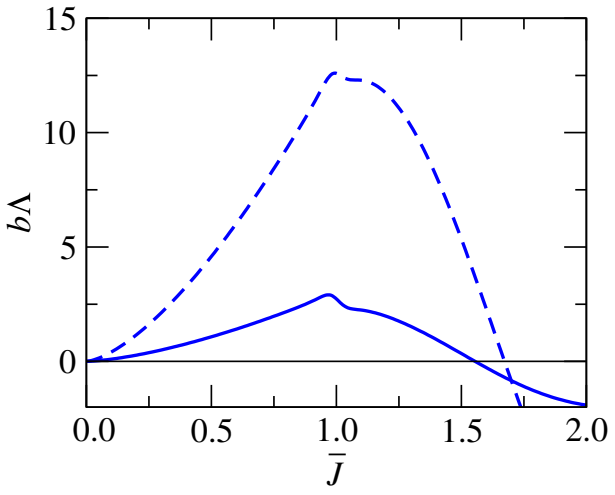

FIG. 3. Parameter $b\Lambda$ versus normalized bias current $\overline{J}$ for different structura1 parameters: $l_g = 0.5$ μm, $\mu_g = 50$ meV, and $\tau_g = 1$ ps (solid line), and $l_g = 0.5$ μm, $\mu_g = 15$ meV, and $\tau_g = 2$ ps (dashed line).

The small breaks in the plots of $b\Lambda$ versus $\overline{J}$ near $\overline{J} = 1$ are attributed to the inclusion of optical-phonon emission at this point. This optical-phonon emission, which starts from $\overline{J} \simeq 1$ (and $\overline{\Phi} \simeq 1$), results in a drop in $b\Lambda$ at larger values of $\overline{J}$. This is because an increase in $\overline{J}$ leads to a relatively smooth increase in $K(\overline{J})$ (and $\overline{\Phi}$) beyond the optical-phonon emission threshold [see Eq. (11)]. When $\overline{J} \gtrsim 1$ ($\overline{\Phi} \gtrsim 1$), only the BCs generated near the gated regions have sufficient energy to emit an optical phonon. The BCs generated in the bulk of the i region are able to do that only at higher values of $\overline{J}$. This is in contrast with the situation in GBFETs [7,8], where the optical-phonon emission threshold is rather sharp.

It should be mentioned that the difference in the values of Λ for the different Fermi energies under consideration is rather small, while the quantity $b\Lambda$ is fairly sensitive to the Fermi energy. This is because $b \propto \mu_g^{-1}$.

V. ac CURRENT AND IMPEDANCE

When $V = \overline{V} + \delta V \exp(-i\omega t)$, where δV and ω are the signal amplitude and frequency, the potential drop across the depleted region and the normalized terminal current comprise the ac components $\delta\Phi$ and $\delta J = \delta J_{\rm BC}/J_0$, respectively. Using Eqs. (3)–(5), the ac normalized current components $\delta J_{\rm DQC}$ can be presented as

$$\frac{\delta J_{\rm EC} + \delta J_{\rm DP}}{J_0} \simeq \frac{2\eta}{3\overline{J}^{1/3}}\left[-\frac{1}{(1-i\omega\tau_g)} + i\omega\tau_{\rm rc}\right]\delta J + \eta\left[-\frac{1}{(1-i\omega\tau_g)} + i\omega\tau_{\rm rc}\right]\frac{\delta V}{V_0}, \quad (15)$$

where $\tau_{\rm rc} = (2l_g c_g/\sigma_g)$ is the gate recharging time, and where the relation $\mathcal{L}_g = (l_g m_g/e^2\Sigma_g) = l_g\tau_g$ is used.

Using Eq. (5), the ac normalized drag current can be presented as

$$\delta J_{\rm DEC} \simeq b\Lambda\,\delta J. \quad (16)$$

Considering this, the linearized version of Eq. (1) together with Eqs. (15) and (16) yields

$$\delta J\left\{1 - b\Lambda + \frac{2\eta}{3\overline{J}^{1/3}}\left[\frac{1}{(1-i\omega\tau_g)} - i\omega\tau_{\rm rc}\right]\right\} = \eta\left[\frac{1}{(1-i\omega\tau_g)} - i\omega\tau_{\rm rc}\right]\frac{\delta V}{V_0}. \quad (17)$$

Equation (17) can be presented in the following form:

$$\delta J = \frac{1 + i\mathcal{F}_\omega}{\left[\frac{3\overline{J}^{1/3}(1-b\Lambda)}{2\eta}(1+\omega^2\tau_g^2) + 1 + i\mathcal{F}_\omega\right]}\frac{\delta V}{V_0}. \quad (18)$$

Here,

$$\mathcal{F}_\omega = \frac{\omega}{\Omega^2\tau_g}[(\Omega^2 - \omega^2)\tau_g^2 - 1], \quad (19)$$

where

$$\Omega = \frac{1}{\sqrt{\tau_g\tau_{\rm rc}}} = \sqrt{\frac{8\pi e^2\Sigma_g d}{\kappa m_g l_g^2}} = \frac{e}{\hbar l_g}\sqrt{\frac{8\mu_g d}{\kappa}} \quad (20)$$

is the plasma frequency of the gated carrier system. One can see that $\Omega = 1/\sqrt{c_g\mathcal{L}_g}$.

Taking the load resistances into account, we arrive at the following expression for the GTTS impedance Z_ω normalized by the resistance of the depleted i region r_i:

$$\frac{Z_\omega}{r_i} = \frac{3\overline{J}^{1/3}(1-b\Lambda)(1+\omega^2\tau_g^2)}{2\eta(1+i\mathcal{F}_\omega)} + 1 + \rho, \quad (21)$$

where

$$r_i H = \frac{1}{\alpha_i\sqrt{V_0}} = 2\pi^2\left(\frac{\hbar v_W}{e^2}\right)\sqrt{\frac{2l_i}{\omega_0\, v_W}}, \quad (22)$$

$\rho = 2r_a/r_i$ (where $2r_a$ is the radiation resistance of the antenna) [see Fig. 1(d)], and H is the GTTS width. In the

range $\overline{J} \leq 1$, Eqs. (13) and (21) result in

$$\frac{Z_\omega}{r_i} = \frac{3\overline{J}^{1/3}}{2\eta}\left(1 - \frac{5b}{2}\overline{J}^{2/3}\right)\frac{(1+\omega^2\tau_g^2)}{(1+i\mathcal{F}_\omega)} + 1 + \rho. \quad (23)$$

As follows from Eqs. (21) and (23), the real part of the GTTS impedance can become negative if

$$\frac{5}{2}b > 1 + \frac{2}{3}\frac{\eta}{(1+\omega^2\tau_g^2)}. \quad (24)$$

For high signal frequencies ($\omega^2\tau_g^2 \gg 1$), the condition described by the inequality in Eq. (24) is much more liberal than the condition in Eq. (13) for S-shaped I-V characteristics. This implies that the real part of the GTTS impedance can be negative with monotonic dc I-V characteristics. It is remarkable that for moderate values of b satisfying the inequality in Eq. (24), but insufficient to satisfy the condition in Eq. (13), $|\delta\Phi|$ can exceed δV, while $\overline{\Phi} < \overline{V}$. This corresponds to the potential profile shown in Fig. 1(c) for the signal component but to the potential profile shown in Fig. 1(b) for the dc component. The inclusion of the load resistance changes the above criteria somewhat, but not by very much (see below).

The condition in Eq. (24) for $(1+\omega^2\tau_g^2) \gg \eta$ yields $b > 2.5$, when the drag effect is essential but not particularly strong. Assuming $\omega/2\pi = 1$ THz and $\tau_g =$ 1 ps, we obtain $(1+\omega^2\tau_g^2) = 1 + 4\pi^2 \simeq 40.5$. For $2l_i =$ 0.1 μm, Eq. (8) yields $J_0 \simeq 1.5$ A/cm. Setting the GTTS width equal to $H =$ (5–10) μm, we find that $r_i/H \simeq$ (133–266)Ω, with $|\mathrm{Re}\, Z_\omega|$ markedly exceeding the latter values.

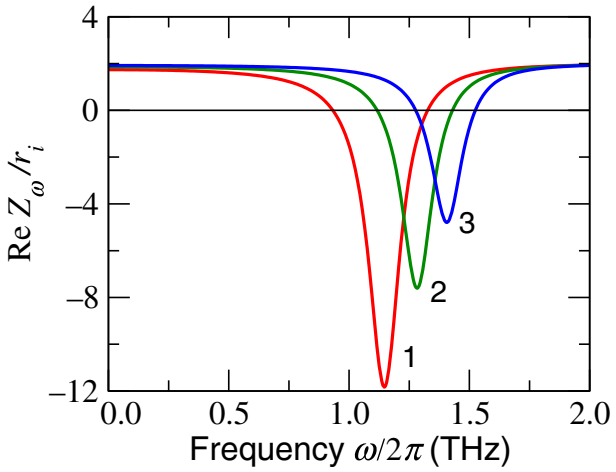

FIG. 4. Real part $\mathrm{Re}\, Z_\omega/r_i$ of the GTTS impedance versus signal frequency $f = \omega/2\pi$ for $\tau_g = 1$ ps, $l_g = 0.5$ μm, $\rho = 1$, and $\overline{J} = 1$ for different structural parameters: 1, $\mu_g = 40$ meV and $\Omega/2\pi = 1.15$ THz; 2, $\mu_g = 50$ meV and $\Omega/2\pi = 1.3$ THz; and 3, $\mu_g = 60$ meV and $\Omega/2\pi = 1.4$ THz.

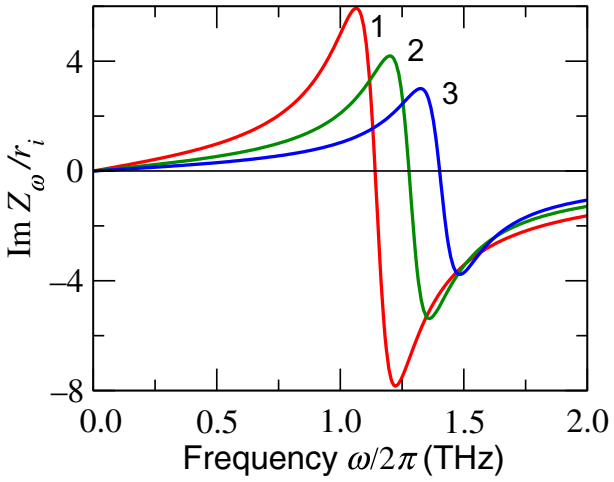

FIG. 5. Imaginary part $\mathrm{Im}\, Z_\omega/r_i$ of the GTTS impedance versus signal frequency $f = \omega/2\pi$. The parameters are the same as in Fig. 4.

Figures 4 and 5 show the frequency dependences of the normalized real and imaginary parts of the GTTS impedance calculated using Eq. (21) with Eq. (12) for different structural parameters.

VI. PLASMA RESONANCE AND PLASMA INSTABILITY

At a signal frequency $\omega = \sqrt{(\Omega^2 - \tau_g^{-2})} = \Omega_p$ corresponding to the plasmonic resonance, $\mathcal{F}|_{\omega=\Omega_p} = 0$. In this case, Eq. (21) yields the following for the resonant impedance $Z_\omega|_{\omega=\Omega_p} = Z_\Omega$:

$$\frac{Z_\Omega}{r_i} = \frac{3\overline{J}^{1/3}(1-b\Lambda)\Omega^2\tau_g^2}{2\eta} + 1 + \rho. \quad (25)$$

Figure 6 shows the real part of the GTTS impedance at a signal frequency coinciding with the plasma frequency Ω (the imaginary part is equal to zero) as a function of the normalized bias current $\overline{J}$. One can see that $|Z_\Omega|$ can be fairly large, which is beneficial for a plasma instability leading to effective THz emission (see below). Moreover, the range of bias currents corresponding to $\mathrm{Re}\, Z_\Omega < 0$ extends markedly into the range $\overline{J} > 1$. This is attributed to a smooth roll-off of the parameter Λ in this range, as seen in Fig. 3.

As is known (see, for example, Ref. [27]), the current in a system with a negative real part of the impedance and with the imaginary part of the latter changing sign can be unstable, resulting in self-excitation of high-frequency oscillations of the carrier density and current (a plasma instability [28]). Such current oscillations, when feeding an antenna, can lead to radiation emission. According to Figs. 4 and 5, the frequency of the emitted radiation can be in the THz range.

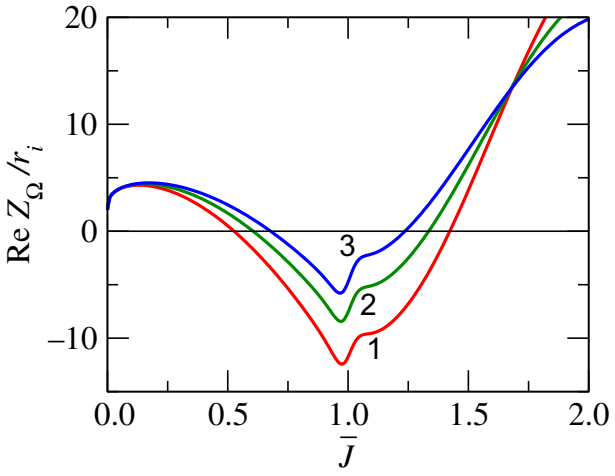

FIG. 6. Real part of the normalized GTTS impedance $\mathrm{Re}\, Z_\Omega/r_i$ at the plasma frequency ($\omega = \Omega$) versus normalized bias current $\overline{J}$ for different plasma frequencies: 1, $\Omega/2\pi = 1.15$ THz; 2, $\Omega/2\pi = 1.3$ THz; and 3, $\Omega/2\pi = 1.4$ THz. The other parameters are the same as in Figs. 4 and 5.

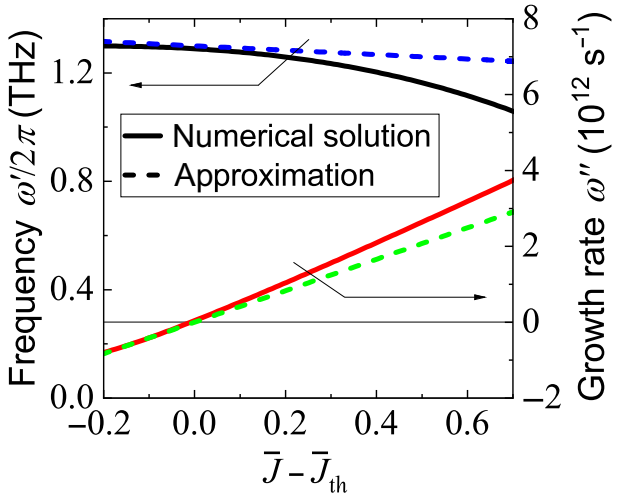

FIG. 7. Real (ω') and imaginary (ω'') parts of the complex signal frequency as functions of the deviation of the bias current $\overline{J}$ from its instability-threshold value $\overline{J}_{\mathrm{th}}$ for $\tau_g = 1$ ps, $l_g = 0.5$ μm, $\mu_g = 50$ meV, $\Omega/2\pi = 1.3$ THz, and $\rho = 1$ (i.e., for $b = 1.25$ and $\eta = 12.56$).

The conditions for this plasma instability and the growth rate of the plasma and current oscillations can be found from the dispersion equation $Z_\omega = 0$ with a complex frequency $\omega = \omega' + i\omega''$, where ω'' represents the growth rate. Using Eq. (23), for $\Omega^2\tau_g^2 \gg 1$ and $\Omega^2\tau_g^2 > \eta$ (so that $\Omega_p \simeq \Omega$), we arrive at the following from the equations $\mathrm{Re}\, Z_{\omega'+i\omega''} = 0$ and $\mathrm{Im}\, Z_{\omega'+i\omega''} = 0$:

$$\frac{\omega'}{\Omega} \simeq 1 - \frac{5b}{4\eta(1+\rho)}(\overline{J} - \overline{J}_{\mathrm{th}}) \simeq 1 - \frac{5b}{4\eta(1+\rho)^2}\frac{(\overline{V} - \overline{V}_{\mathrm{th}})}{V_0}, \tag{26}$$

$$\frac{\omega''}{\Omega} \simeq \frac{5b\Omega\tau_g}{4\eta(1+\rho)}(\overline{J} - \overline{J}_{\mathrm{th}}) \simeq \frac{5b\Omega\tau_g}{4\eta(1+\rho)^2}\frac{(\overline{V} - \overline{V}_{\mathrm{th}})}{V_0}. \tag{27}$$

Here, $V_{\mathrm{th}}/V_0 = (1+\rho)r_i J_0 \overline{J}_{\mathrm{th}}/V_0 = (1+\rho)\overline{J}_{\mathrm{th}}$, where $\overline{J}_{\mathrm{th}}$ represents the normalized threshold current, obeying the following equation:

$$\overline{J}_{\mathrm{th}}^{1/3} - \frac{5b}{2}\overline{J}_{\mathrm{th}} = -\frac{2\eta(1+\rho)}{3\Omega^2\tau_g^2}. \tag{28}$$

Equation (28) yields

$$\overline{J}_{\mathrm{th}} \simeq \left(\frac{2}{5b}\right)^{3/2}\left[1 + \left(\frac{5b}{2}\right)^{1/2}\frac{\eta(1+\rho)}{\Omega^2\tau_g^2}\right]. \tag{29}$$

Hence

$$\frac{\overline{V}_{\mathrm{th}}}{V_0} \simeq (1+\rho)\left(\frac{2}{5b}\right)^{3/2}\left[1 + \left(\frac{5b}{2}\right)^{1/2}\frac{\eta(1+\rho)}{\Omega^2\tau_g^2}\right]. \tag{30}$$

As follows from Eqs. (26) and (27), when $\overline{V}$ exceeds the threshold value $\overline{V}_{\mathrm{th}}$, the plasma oscillations become unstable, with a growth rate $\omega'' > 0$. The plasma instability threshold ($\omega'' = 0$) corresponds to $\omega' = \Omega_p \simeq \Omega$.

The inequalities $V_{\mathrm{th}} < \overline{V} \leq V_0(1+\rho)$, i.e., $\overline{J}_{\mathrm{th}} < \overline{J} \leq 1$, and $\omega'' > 0$ constitute necessary and sufficient conditions for a plasma instability [compare the inequality in Eq. (24), which is the pertinent necessary condition]. One can see that for a sufficiently large load resistance ($\rho \gg 1$), the plasma instability vanishes, i.e., the plasma oscillations become damped. The proportionality of the growth of the plasma oscillations to the drag factor b seen in Eq. (27) shows that the plasma instability under consideration is linked to the drag effect. When b tends to zero, $\overline{J}_{\mathrm{th}}$ and $\overline{V}_{\mathrm{th}}$ tend to infinity.

Figure 7 illustrates the dependence of ω' and ω'', i.e., the frequency of the self-excited plasma oscillations and their growth rate, on $(\overline{J} - \overline{J}_{\mathrm{th}})$, calculated numerically (solid lines) using the equations $\mathrm{Re}\, Z_{\omega'+i\omega''} = 0$ and $\mathrm{Im}\, Z_{\omega'+i\omega''} = 0$, with Z_ω given by Eq. (23). The dashed lines in Fig. 7 correspond to an analytic approximation obtained from Eqs. (26), (27), and (29).

VII. COMMENTS

Above, as in Refs. [7,8], we disregard the delay due to the flight of the BCs across the *i* region and, hence, the pertinent transit-time effects [5,6,29]. Such effects could also

be responsible for the self-excitation of oscillations at the transit-time frequency $\omega \sim \omega_{tr} = 2\pi v_W/l_i$ [5] and could, in principle, affect the instability mechanism considered in the present paper. However, for $\omega < \omega_{tr}$, the omission of the transit-time delay in the i region is justified. Indeed, for the main parameters used in the above calculations, $\omega_{tr}/2\pi \simeq 10$ THz, while in the above $\omega/2\pi$ and $\Omega/2\pi$ are about 1 THz, i.e., $\omega, \Omega \ll \omega_{tr}$.

The parameter crucial for the dc I-V characteristics and high-frequency performance of devices using Coulomb carrier drag is the characteristic current density J_0. Comparing J_0 with the pertinent density for GBFETs $J_0^{(GBFET)}$ [7,8] we obtain

$$\frac{J_0}{J_0^{(GBFET)}} = \frac{e^2 l_i^{(GBFET)}}{\pi\kappa\hbar v_W}\sqrt{\frac{\omega_0}{2l_i v_W}}.$$

Setting $\kappa = 4$–6 and assuming equal lengths of the i region ($l_i^{GBFET} = 2l_i = 0.1$ μm) and the gated regions, we obtain $J_0/J_0^{(GBFET)} \simeq 0.7$–$1.0$. This implies that GTTSs and GBFETs exhibit similar characteristics.

GTTSs, in comparison with GBFETs, are characterized by a smaller drag factor (twice as small for the same carrier scattering time in the gated region). This is because, in the former case, the average energy and momentum of the injected BCs are equal to $eV/2$ and $eV/2v_W$, respectively, i.e., in GBFETs with thermionic emission from the source contact, the drag factor in a GTTS is 2 times smaller (for the same gated-region length). However, this is compensated by a smoother decrease in Λ beyond the optical-phonon emission threshold. The latter also leads to a wider span, ΔJ, of the bias current in which the real part of the impedance can be negative compared with GBFETs. In particular, the impedance of a GTTS can be negative at $\overline{J} > 1$, while the impedance of a GBFET becomes positive once $\overline{J} \geq 1$. The quantity ΔJ determines the characteristic (maximum) output THz power emitted by a GTTS. For $2l_i = 0.1$ μm, assuming $J_0 \simeq 1.5$ A/cm and a GTTS width $H = 10$ μm, $r_i = 200/1.5 \simeq 133$ Ω, and $\Omega/2\pi = 1.15$ THz. Hence, as follows from Fig. 6, for $|Z_\Omega| = 2r_i \simeq 266$ Ω one can find $H\,\Delta J \simeq 0.75 H J_0 \simeq 1.125$ mA. As a result, for an impedance-matched antenna radiation resistance equal to $2r_a = |Z_\Omega| = 266$ Ω, the characteristic emitted THz power satisfies $P_\omega \simeq 337.5$ μW, or $P_\omega/H \simeq 37.5$ mW/mm.

The sensitivity of the GTTS characteristics to several parameters opens up wide opportunities for their optimization. The fact that in GTTSs the tunneling injection occurs in the bulk of the i region can be considered as an advantage (in comparison with GBFETs), since it weakens the requirements on the quality of the side contacts.

Devices based on GTTS structures with chemically doped regions can exhibit similar phenomena to gated GTTSs with electrostatic doping of the p and n regions. To avoid excessive scattering of the BCs on ionized dopants, the acceptors and donors should not be placed too close to the channel (selective remote doping). The plasma frequency in ungated structures can be markedly larger than in gated GTTSs for the same lengths of the p and n regions. Shortening these regions is beneficial for enhancement of the drag factor b and, hence, reinforces the drag-related effects.

Further development of GTTS-based devices using Coulomb carrier drag can be achieved using periodic structures with p^+-i-n^+ GTTSs connected in series (with reverse-biased p^+-i-n^+ GTTSs and forward-biased n^+-p^+ junctions connecting neighboring GTTSs in series [30,31])—the cascade GTTS. In such periodic structures, one can expect reinforced THz emission and the self-excitation of propagating plasma waves (associated with the plasma instability considered above) with periods equal to multiples of the period of the structure, resulting in additional functionality. Vertical integration of p^+-i-n^+ GTTSs with non-Bernal stacked (twisted) G layers or G layers separated by dielectric layers such as h-BN layers [6,32,33] could also promote the enhancement of the efficiency of GTTS THz radiation sources (see also Ref. [34]).

Early attempts to predict and realize THz plasma instabilities in different semiconductor devices are well documented in the literature (see, for example, Refs. [35–41]). The most popular idea was to use streams of different groups of carriers to model the situation in gaseous plasmas [42]. Similar concepts were revived in applications to G-based heterostructures [43–45] (see also a critical analysis of the pertinent problem [46]). The main obstacle to realizing two-stream plasma instabilities in semiconductor heterostructures is associated with difficulties in creating plasma systems with a sufficiently large directed velocity of at least one carrier component (in particular, ballistic transport of this component) maintained along a relatively long channel under conditions of marked carrier-carrier collisions. In this regard, plasma instabilities associated with positive feedback due to the reflection of plasma waves and carriers from the side contacts [the Dyakonov-Shur (DS) instability [47]] might require much more liberal conditions. In particular, the observed plasma instability in dual-grating G-based structures [48,49] is attributed to the occurrence of a DS instability supported by a carrier-transit-time effect [29,50]. The instability associated with positive feedback between BCs injected from a GBFET source [7] or with BCs tunnel-generated in the depleted region of a GTTS (studied above), on the one hand, and the reverse injection of ECs caused by the Coulomb drag effect, on the other, can be considered as belonging to the same class as the DS instability. Although the realization of the plasma instability under consideration requires ballistic carrier transport in the i region, which is assumed to be fairly short ($2l_i \sim 0.1$ μm), in the gated regions occupied by ECs, the carrier mean free path (limited by

carrier-carrier collisions) can be substantially shorter than the length l_g of this region. The latter is a much more practical condition than in situations in which a two-stream instability might be possible.

VIII. CONCLUSIONS

In conclusion, we predict a current-driven plasma instability in a lateral GTTS with carrier injection into the gated p and n regions and Coulomb drag of ECs by BCs. The plasma instability and the related emission of THz radiation are associated with current amplification due to the transfer of the momentum of BCs to ECs. Lateral GTTS cascades and vertically integrated GTTSs can exhibit enhanced THz emission and widen the range of functionality of GTTSs. GTTSs can be effective THz sources, surpassing existing nanostructure emitters.

The data that support the findings of this study are available from the corresponding author [51] upon reasonable request.

ACKNOWLEDGMENTS

The work at RIEC and UoA was supported by the Japan Society for Promotion of Science (KAKENHI Grants No. 21H04546 and No. 20K20349), Japan, and the RIEC Nation-Wide Collaborative Research Project No. H31/A01, Japan. The work at RPI was supported by the Office of Naval Research (Grant No. N000141712976, Project Monitor Dr. Paul Maki).

[1] V. V. Cheianov and V. I. Fal'ko, Selective transmission of Dirac electrons and ballistic magnetoresistance of n-p junctions in graphene, Phys. Rev. **74**, 041103 (2006).

[2] A. Ossipov, M. Titov, and C. W. J. Beenakker, Reentrance effect in a graphene n-p-n junction coupled to a superconductor, Phys. Rev. B **75**, 241401(R) (2007).

[3] D. Jena, Tunneling transistors based on graphene and 2-D crystals, Proc. IEEE **101**, 1585 (2013).

[4] N. Vandecasteele, A. Barreiro, M. Lazzeri, A. Bachtold, and F. Mauri, Current-voltage characteristics of graphene devices: Interplay between Zener-Klein tunneling and defects, Phis. Rev. B **82**, 045416 (2010).

[5] V. Ryzhii, M. Ryzhii, V. Mitin, and M. S. Shur, Graphene tunneling transit-time terahertz oscillator based on electrically induced p-i-n junction, Appl. Phys. Exp. **2**, 034503 (2009).

[6] V. L. Semenenko, V. G. Leiman, A. V. Arsenin, V. Mitin, M. Ryzhii, T. Otsuji, and V. Ryzhii, Effect of self-consistent electric field on characteristics of graphene p-i-n tunneling transit-time diodes, J. Appl. Phys. **113**, 024503 (2013).

[7] V. Ryzhii, M. Ryzhii, V. Mitin, M. S. Shur, and T. Otsuji, S-Shaped Current-Voltage Characteristics of n^+-i-n-n^+ Graphene Field-Effect Transistors due the Coulomb Drag of Quasi-Equilibrium Electrons by Ballistic Electrons, Phys. Rev. Appl. **16**, 014001 (2021).

[8] V. Ryzhii, M. Ryzhii, V. Mitin, M. S. Shur, and T. Otsuji, Coulomb electron drag mechanism of terahertz plasma instability in n+-i-n-n+ graphene FETs with ballistic injection, Appl. Phys. Lett. **119**, 093501 (2021).

[9] J. C. Song, D. A. Abanin, and L. S. Levitov, Coulomb drag mechanisms in graphene, Nano Lett. **13**, 3631 (2013).

[10] M. Schütt, P. M. Ostrovsky, M. Titov, I. V. Gornyi, B. N. Narozhny, and A. D. Mirlin, Coulomb Drag in Graphene near the Dirac Point, Phys. Rev. Lett. **110**, 026601 (2013).

[11] R. V. Gorbachev, A. K. Geim, M. I. Katsnelson, K. S. Novoselov, T. Tudorovskiy, I. V. Grigorieva, A. H. MacDonald, S. V. Morozov, K. Watanabe, T. Taniguchi, and L. A. Ponomarenko, Strong Coulomb drag and broken symmetry in double-layer graphene, Nat. Phys. **8**, 896 (2012).

[12] V. Vyurkov and V. Ryzhii, Effect of Coulomb scattering on graphene conductivity, JETP Lett. **88**, 370 (2008).

[13] X. Li, E. A. Barry, J. M. Zavada, M. Buongiorno Nardelli, and K. W. Kim, Influence of electron-electron scattering on transport characteristics in monolayer graphene, Appl. Phys. Lett. **97**, 082101 (2010).

[14] D. Svintsov, V. Vyurkov, S. Yurchenko, T. Otsuji, and V. Ryzhii, Hydrodynamic model for electron-hole plasma in graphene, J. Appl. Phys. **111**, 083715 (2012).

[15] D. Svintsov, V. Vyurkov, V. Ryzhii, and T. Otsuji, Hydrodynamic electron transport and nonlinear waves in graphene, Phys. Rev. B **88**, 245444 (2013).

[16] F. Bianco, D. Perenzoni, D. Convertino, S. L. De Bonis, D. Spirito, M. Perenzoni, C. Coletti, M. S. Vitiello, and A. Tredicucci, Terahertz detection by epitaxial-graphene field-effect transistors on silicon carbide, Appl. Phys. Lett. **107**, 131104 (2015).

[17] D. Yadav, S. Boubanga-Tombet, T. Watanabe, S. Arnold, V. Ryzhii, and T. Otsuji, Terahertz wave generation and detection in double-graphene layered van der waals heterostructures, 2D Mater. **3**, 045009 (2016).

[18] D. Yadav, G. Tamamushi, T. Watanabe, J. Mitsushio, Y. Tobah, K. Sugawara, A. A. Dubinov, A. Satou, M. Ryzhii, V. Ryzhii, and T. Otsuji, Terahertz light-emitting graphene-channel transistor toward single-mode lasing, Nanophotonics **7**, 741 (2018).

[19] S. Boubanga-Tombet, W. Knap, D. Yadav, A. Satou, D. B. But, V. V. Popov, I. V. Gorbenko, V. Kachorovskii, and T. Otsuji, Room Temperature Amplification of Terahertz Radiation by Grating-Gate Graphene Structures, Phys. Rev. X **10**, 031004 (2020).

[20] J. A. Delgado-Notario, V. Clericò, E. Diez, J. E. Vel'azquez-P'erez, T. Taniguchi, K. Watanabe, T. Otsuji, and Y. M. Meziani, Asymmetric dual grating gates graphene FET for detection of terahertz radiations, APL Photon **5**, 066102 (2020).

[21] P. Padmanabhan, S. Boubanga-Tombet, H. Fukidome, T. Otsuji, and R. P. Prasankumar, A graphene-based magnetoplasmonic metasurface for actively tunable transmission and polarization rotation at terahertz frequencies, Appl. Phys. Lett. **116**, 221107 (2020).

[22] K. Shiga, T. Komiyama, Y. Fuse, H. Fukidome, A. Satou, T. Otsuji, and T. Uchino, Electrical transport properties of gate tunable graphene lateral tunnel diodes, Jpn. J. Appl. Phys. **59**, SIID03 (2020).

[23] Q. Wilmart, M. Boukhicha, H. Graef, D. Mele, J. Palomo, M. Rosticher, T. Taniguchi, K. Watanabe, V. Bouchiat, E. Baudin, J.-M. Berroir, E. Bocquillon, G. Feve, E. Pallecchi, and B. Plaçais, High-frequency limits of graphene field-effect transistors with velocity saturation, Appl. Sci. **10**, 446 (2020).

[24] A. S. Mayorov, R. V. Gorbachev, S. V. Morozov, L. Britnell, R. Jalil, L. A. Ponomarenko, P. Blake, K. S. Novoselov, K. Watanabe, T. Taniguchi, and A. K. Geim, Micrometer-scale ballistic transport in encapsulated graphene at room temperature, Nano Lett. **11**, 2396 (2011).

[25] L. Banszerus, M. Schmitz, S. Engels, M. Goldsche, K. Watanabe, T. Taniguchi, B. Beschoten, and C. Stampfer, Ballistic transport exceeding 28 μm in CVD grown graphene, Nano Lett. **16**, 1387 (2016).

[26] M. V Fischetti, J Kim, S. Narayanan, Z.h.-Y. Ong, C. Sachs, D. K. Ferry, and S. J. Aboud, Pseudopotential-based studies of electron transport in graphene and graphene nanoribbons, J Phys: Cond. Mat. **25**, 473202 (2013).

[27] G. I. Haddad, J. R. East, and H. Eisele, Two-terminal active devices for terahertz sources, Int. J. High Speed Electron. Syst. **13**, 395 (2003).

[28] G. R. Aizin, J. Mikalopas, and M. Shur, Plasmonic instabilities in two-dimensional electron channels of variable width, Phys. Rev. B **101**, 245404 (2020).

[29] V. Ryzhii, A. Satou, and M. S. Shur, Plasma instability and terahertz generation in HEMTs electron transit-time effect, IEICE Trans. Electron. **E89-C**, 1012 (2006).

[30] T. A. Elkhatib, V. Y. Kachorovskii, W. J. Stillman, D. B. Veksler, K. N. Salama, Xi-Ch. Zhang, and M. S. Shur, Enhanced plasma wave detection of terahertz radiation using multiple high electron-mobility transistors connected in series, IEEE Trans. Microwave Theory Tech. **58**, 331 (2010).

[31] V. Ryzhii, M. Ryzhii, A. Satou, N. Ryabova, T. Otsuji, V. Mitin, F. T. Vasko, A. A. Dubinov, V. Y. Aleshkin, and M. S. Shur, in *Future Trends in Microelectronics*, ed. by S. Luryi, J. Xu, and A. Zaslavsky, Wiley, 2010, p. 293.

[32] Y. Sui and J. Appenzeller, Screening and interlayer coupling in multilayer graphene field-effect transistors, Nano Lett. **9**, 2973 (2009).

[33] M. Ryzhii, V. Ryzhii, T. Otsuji, V. Mitin, and M. S. Shur, Electrically induced n-i-p junctions in multiple graphene layer structures, Phys. Rev. B **82**, 075419 (2010).

[34] M. Shur, G. Aizin, T. Otsuji, and V. Ryzhii, Plasmonic field effect transistors (TeraFETs) for 6G communications, Sensors (MDPI), in press.

[35] B. B. Robinson and G. A. Swartz, Two-stream instability in semiconductor plasmas, J. Appl. Phys. **38**, 2461 (1967).

[36] M. V. Krasheninnikov and A. V. Chaplik, Instabilities of two-dimensional plasma waves, Sov. Phys. JETP **52**, 279 (1980).

[37] P. Hawrylak and J. J. Quinn, Amplification of bulk and surface plasmons in semiconductor superlattices, Appl. Phys. Lett. **49**, 280 (1986).

[38] P. Bakshi, J. Cen, and K. Kempa, Amplification of surface modes in type II semiconductor superlattices, J. Appl. Phys. **64**, 2243 (1988).

[39] B. Y.-K. Hu and J. W. Wilkins, Two-stream instabilities in solid-state plasmas caused by conventional and unconventional mechanisms, Phys. Rev. B **43**, 14009 (1991).

[40] Z. S. Gribnikov, N. Z. Vagidov, and V. V. Mitin, Two-stream instability and oscillatory regimes induced in ballistic diodes and field-effect transistors, J. Appl. Phys. **88**, 6736 (2000).

[41] S. Riyopoulos, THz instability by streaming carriers in high mobility solid-state plasmas, Phys. Plasmas **12**, 070704 (2005).

[42] G. D. Boyd, L. M. Field, and R. W. Gould, Excitation of plasma oscillations and growing plasma waves, Phys. Rev. **109**, 1393 (1958).

[43] C. M. Aryal, B. Y.-K. Hu, and A.-P. Jauho, Plasma wave instabilities in nonequilibrium graphene, Phys. Rev. B **94**, 115401 (2016).

[44] Ch. M. Aryal, B. Yu-K. Hu, and A.-P. Jauho, Plasma wave instabilities in nonequilibrium graphene, Phys. Rev. B **94**, 115401 (2016).

[45] T. A. Morgado and M. G. Silveirinha, Negative Landau Damping in Bilayer Graphene, Phys. Rev. Lett. **119**, 133901 (2017).

[46] D. Svintsov and V. Ryzhii, Comment on "Negative Landau Damping in Bilayer Graphene", Phys. Rev. Lett. **123**, 219401 (2019).

[47] M. Dyakonov and M. Shur, Shallow Water Analogy for a Ballistic Field Effect Transistor: New Mechanism of Plasma Wave Generation by dc Current, Phys. Rev. Lett. **71**, 2465 (1993).

[48] Y. Koseki, V. Ryzhii, T. Otsuji, V. V. Popov, and A. Satou, Giant plasmon instability in a dual-grating-gate graphene field-effect transistor, Phys. Rev. B **93**, 245408 (2016).

[49] S. Boubanga-Tombet, W. Knap, D. Yadav, A. Satou, D. B. But, V. V. Popov, I. V. Gorbenko, V. Kacharovskii, and T. Otsuji, Room-Temperature Amplification of Terahertz Radiation by Grating-Gate Graphene Structures, Phys. Rev. X **10**, 031004 (2020).

[50] V. Ryzhii, A. Satou, and M. S. Shur, Transit-time mechanism of plasma instability in high electron mobility transistors, Phys. Status Solidi A **202**, R113 (2005).

[51] V. Ryzhii, v-ryzhii@riec.tohoku.ac.jp.